Faraday Discussions

Accepted Manuscript

This manuscript will be presented and discussed at a forthcoming Faraday Discussion meeting. All delegates can contribute to the discussion which will be included in the final volume.

Register now to attend! Full details of all upcoming meetings: http://rsc.li/fd-upcoming-meetings

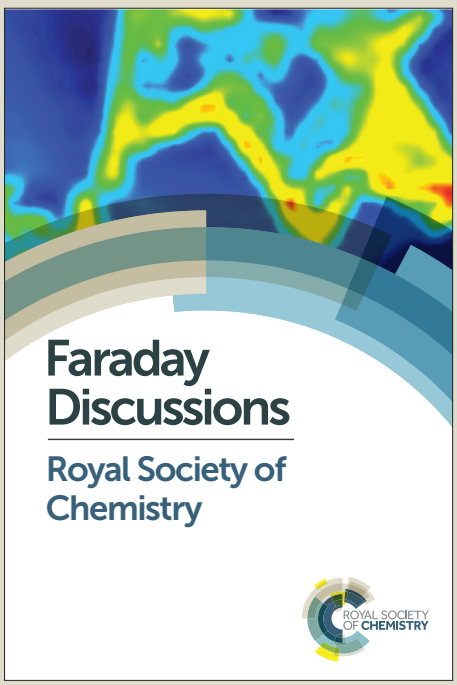

This is an *Accepted Manuscript*, which has been through the Royal Society of Chemistry peer review process and has been accepted for publication.

Accepted Manuscripts are published online shortly after acceptance, before technical editing, formatting and proof reading. Using this free service, authors can make their results available to the community, in citable form, before we publish the edited article. We will replace this *Accepted Manuscript* with the edited and formatted *Advance Article* as soon as it is available.

You can find more information about *Accepted Manuscripts* in the Information for Authors.

Please note that technical editing may introduce minor changes to the text and/or graphics, which may alter content. The journal's standard Terms & Conditions and the Ethical guidelines still apply. In no event shall the Royal Society of Chemistry be held responsible for any errors or omissions in this *Accepted Manuscript* or any consequences arising from the use of any information it contains.

ROYAL SOCIETY OF CHEMISTRY

www.rsc.org/faraday_d

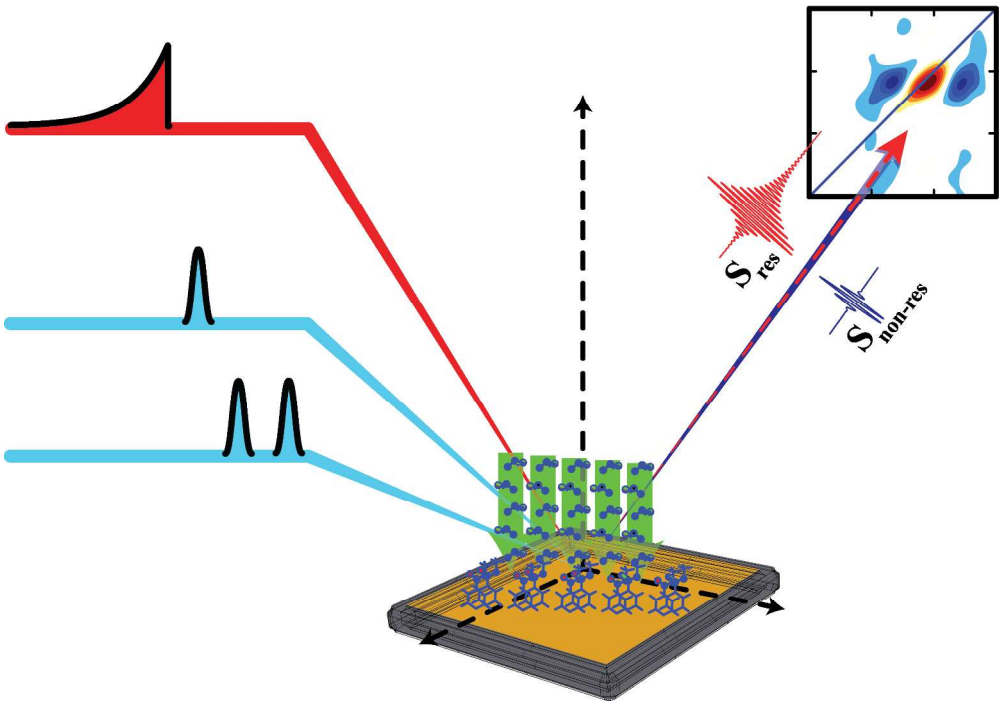

Two-dimensional sum-frequency generation (2D SFG) spectroscopy: Summary of principles and its application to amyloid fiber monolayers

Ayanjeet Ghosh, Jia-Jung Ho, Arnaldo L. Serrano, David R. Skoff, Tianqi Zhang and Martin T. Zanni

Department of Chemistry, University of Wisconsin, 1101 University Avenue, Madison, WI 53706 (USA), Tel: 608 262 4783, Email: zanni@chem.wisc.edu

DOI: 10.1039/b000000x [DO NOT ALTER/DELETE THIS TEXT]

By adding a mid-infrared pulse shaper to a sum-frequency generation (SFG) spectrometer, we have built a 2D SFG spectrometer capable of measuring spectra analogous to 2D IR spectra but with monolayer sensitivity and SFG selection rules. In this paper, we describe the experimental apparatus and provide an introduction to 2D SFG spectroscopy to help the reader interpret 2D SFG spectra. The main aim of this manuscript is to report 2D SFG spectra of the amyloid forming peptide FGAIL. FGAIL is a critical segment of the human islet amyloid polypeptide (hIAPP or amylin) that aggregates in people with type 2 diabetes. FGAIL is catalyzed into amyloid fibers by many types of surfaces. Here, we study the structure of FGAIL upon deposition onto a gold surface covered with a self-assembled monolayer of methyl 4-mercaptobenzoate (MMB) that produces an ester coating. FGAIL deposited on bare gold does not form ordered layers. The measured 2D SFG spectrum is consistent with amyloid fiber formation, exhibiting both the parallel (a^+) and perpendicular (a^-) symmetry modes associated with amyloid β-sheets. Cross peaks are observed between the ester stretches of the coating and the FGAIL peptides. Simulations are presented for two possible structures of FGAIL amyloid β-sheets that illustrates the sensitivity of the 2D SFG spectra to structure and orientation. These results provide some of the first molecular insights into surface catalyzed amyloid fiber structure.

Introduction

Humans and animals suffer from diseases caused by aggregated proteins, such as cataracts and type 2 diabetes[1]. The protein involved in type 2 diabetes, called the islet amyloid polypeptide (IAPP or amylin) is particularly interesting because its sequence is conserved across species except for the middle segment spanning residues 20-29.[2] This region includes the FGAIL segment in humans, which forms well-ordered amyloid fibers under many conditions[2-6]. In rats, mice, and other species that do not contract type 2 diabetes, the corresponding FGAIL sequence contains 1 or more mutations that prevent it from aggregating[2]. Thus, there is a standing hypothesis that the FGAIL and nearby amino acids dictate amyloid fiber formation and thus the propensity for contracting type 2 diabetes[2, 4, 6, 7]. That hypothesis is now being questioned and refined by more recent experiments on the full-length protein using solid-state NMR and by 2D IR spectroscopy[8, 9]. Nonetheless, it is clear that the FGAIL sequence plays an important role in dictating amyloid fiber formation.

It is also established that amyloid fiber formation is catalyzed by many types of surfaces[10-12]. IAPP and other amyloid proteins are charged and so are attracted to charged surfaces. Human IAPP is amphipathic. Surfaces, whether or not they are charged, may also serve to effectively increase the protein concentration since diffusion in two rather than three dimensions will more quickly produce protein-protein contacts from which aggregation can commence. Indeed, there are many images collected using atomic force microscopy of amyloid fibers formed on mica and other surfaces[13, 14]. However, the atomic structures of these amyloid fibers are not known and it is not known if these fibers have the same structure as when formed spontaneously without surfaces present. Indeed, polymorphs, which are alternate structures of amyloid fibers formed from different conformations of the same protein, are now recognized as a common phenomena[15], probably because amyloid fibers are kinetically trapped structures that do not ever reach the structure that would be dictated by the thermodynamic minima.

There have been a number experiments and simulations of the FGAIL and NFGAIL segments of IAPP[4, 16-18]. In solution, they form very flat and long fibers, as determined by TEM[4]. Additionally, β-sheet structure was confirmed by FTIR[19]. N-methylated derivatives of these peptides have even been shown to inhibit fibrillation of full length hIAPP[20]. While ssNMR studies on the longer 20-29 segment found the aggregates to form into anti-parallel sheets, and x-ray crystallography has shown NNFGAIL to form parallel sheets[21], no such experiments have been carried out on FGAIL or NFGAIL, and various simulation studies have alternatively predicted either parallel or anti-parallel structure. Interestingly, a recent study found that CFGAILSS forms anti-parallel amyloid fibrils in solution but when constrained to gold nanoparticles surfaces through thiol tethering, it forms parallel sheets[22]. This result exemplifies the importance of surfaces to the detailed structural dynamics of amyloids. In this case, the specific thiol-gold interaction is critical to morphology. Evidence for other specific interactions have been shown to be critical to amyloid morphology: MD simulations on the related NFGAIL fragment and its mutant

NAGAIL highlighted the importance of Phe-Phe T-stacking interactions in the stability of fibrils, as the latter could not form stable oligomers[23]. Such interactions could serve as targets for forming non-covalent monolayers and nanostructures out of naturally self-assembling peptides or for tuning the morphology of a given peptides amyloid structure.

In this article, we collect heterodyne-detected 2D SFG spectra of the FGAIL peptide on a gold surface coated with an ester functional group via the self-assembly of a monolayer of methyl 4-mercaptobenzoate. The goal is to probe the structure of the assembled peptides on these surfaces and to understand the role of hydrophobicity, hydrogen bonding, and ring stacking contacts that could play a role in structure formation. The 2D SFG spectrometer is built by adding a mid-IR pulse shaper to a standard broadband SFG spectrometer. The pulse shaper is used to generate the additional pulse pair from which the second dimension is generated. Phase cycling of the pulse pair is used to set the rotating frame and subtract background noise without having to lose signal from chopping. The spectra are simulated using an excitonic coupling model and selection rules calculated for 2D SFG spectra. The comparison of simulation to experiment provides a preliminary model for the assembly of FGAIL on gold and the ester coated surface.

Introduction to 2D SFG spectroscopy

Sum-frequency generation spectroscopy is one of the most common techniques for studying surfaces and interfaces[24-30]. SFG spectroscopy is a second-order technique in which a resonant mid-IR pulse combines with a non-resonant visible pulse to produce a signal at the sum of the two frequencies[25, 27]. Fig. 1a shows a SFG pulse sequence in which a femtosecond laser pulse is followed by a picosecond visible pulse, as is typical for broadband SFG spectrometer[31] (The envelope of the visible pulse is shown as a decaying exponential as would be generated by a filter. Other methods for creating the narrowband visible pulse would have different shapes in the time-domain.) When the signal is scaled back to the mid-IR by subtracting the visible pulse frequency, one obtains a vibrational spectrum. The frequencies in the spectrum would match those of IR and Raman spectra, if they could be measured, with intensities that scale as a combination of the two since both the vibrational transition dipole and the polarizability contribute. In addition, some modes may not contribute at all if they are isotropically distributed, which is what makes SFG spectroscopy surface selective.

Two modifications are needed to generate a 2D SFG spectrum. First, a 2D spectrum requires a second vibrational frequency-axis to be measured, which necessitates additional infrared laser pulse(s). One can use a picosecond mid-IR laser pulse whose center frequency is scanned, but that limits the time-resolution of the experiment and causes spectral distortions[32]. Early 2D IR experiments used frequency scanning methods, but that has now largely given way to impulsive experiments that only use femtosecond laser pulses[33-35]. Thus, rather than use a

single picosecond mid-IR pulse, we use two femtosecond laser pulses, as shown in Fig. 1a. The time-delay, t_1, between the pulses is scanned and the data Fourier transformed to give the second frequency axis but with no loss in time-resolution and improved lineshapes. Second, the signal must be heterodyne detected, otherwise phase distortions are present that make it difficult to interpret the spectra or to compare to either FTIR or 2D IR spectra which are always heterodyne detected. For the samples studied here, heterodyne detection is automatically accomplished with the non-resonant signal from the gold interface. For non-metallic surfaces, one needs to add an additional pulse commonly called a local oscillator. Because our pulse pairs are generated by a pulse shaper, as described below, they are collinear, resulting in the beam geometry shown in Fig. 1b.

Shown in Fig. 2 are simulated heterodyne-detected 2D SFG spectra for two coupled oscillators, such as would be measured for a small organic molecule, a dipeptide, a DNA base, or any other molecule with two coupled vibrational modes like two carbonyls. Three variations of 2D SFG spectra are shown to illustrate commonly observed features[36]. In the first 2 spectra (Fig. 2a and b), there is a pair of diagonal peaks for each of the vibrational modes, with one peak exactly on the diagonal created by transitions that only include the fundamentals (v=0→1) of each mode and an out-of-phase peak that includes a transition to the overtone (v=1→2). Because of coupling, pairs of cross peaks are also observed that correspond to transitions involving the vibrational modes from both oscillators. The phases of the peak pairs will depend on the directions of the transition dipole and polarizability tensors with respect to the plane of the surface, thereby providing information on the orientation of the molecule (compare Fig. 2a to 2b). If a particular mode is isotropically distributed across the interface, like shown in Fig. 2c, then it will not be SFG active and so will not appear in either 1D SFG or along the diagonal in 2D SFG spectra. However, cross peaks can still appear to SFG forbidden modes. That occurs because an SFG *inactive* mode is still pumped by the mid-IR pulses, and so can emit a signal if it is coupled to an SFG *active* mode. This property is proving very useful for interpreting 2D SFG signals[37, 38].

Experimental Implementation

To implement 2D SFG spectroscopy, we add a mid-IR pulse shaper to a broadband SFG spectrometer. The pulse shaper is used to generate the pair of pump pulses, scan their time delays, and increment their phases for background subtraction and shifting data collection in the rotating frame. A schematic of our apparatus is shown in Fig. 3. It consists of a regeneratively-amplified Ti:Sapphire laser that outputs femtosecond pulses (800 nm, ~50 fs FWHM, ~4 mJ/pulse) at a 1 kHz repetition rate. Three quarters of the 800 nm output (3 mJ/pulse) pumps an optical parametric amplifier with $AgGaS_2$ difference frequency generation to produce about 30 μJ/pulse of mid-IR light centered at 6 μm. A CaF_2 window is used to split the mid-IR pulse into a pump and probe beam path. About 95% of the light is sent through the mid-IR pulse shaper using a transverse Ge acousto-optic modulator to create the pulse pair.

We refer to the two pulses as the E_1 and E_2 pump beams. The remaining 5% is used as the mid-IR probe pulse, E_3. The 800 nm light not used for mid-IR generation (1 mJ/pulse) is frequency-narrowed using a 1 nm FWHM interference filter centered at 805 nm. After filtering, the visible pulse power is 15 μJ/pulse. The visible pulse and mid-IR pulses are focused using 30 cm and 20 cm lenses respectively and overlapped at the sample. The angle of incidence for the visible pulse is θ_{vis} = 65°, and for the mid-IR pulses θ_{IR} = 75° from normal. The visible pulse and all mid-IR pulses are *p*-polarized to collect a ppppp 2D SFG signal. The signal beam is re-collimated and a 735 nm short pass filter is used to remove unwanted 800 nm light. This signal is sent into a monochromator and frequency dispersed onto a CCD detector. To prevent sample degradation during the experiment, the sample was scanned in the *xy*-plane such that a spot on the sample was only probed for 5 minutes (i.e., 5000 laser shots) before changing to a new spot.

Phase cycling, background subtraction, and step sizes

Because the E_1 and E_2 pump beams are collinear, the 4th-order SFG electric field, $E_{res}^{(4)}(\omega_3,t_1,t_2)$ that we want to measure is emitted in the same direction as the 2nd-order SFG field, $E_{res}^{(4)}(\omega_3,t_1,t_2)$, created by E_3 and the visible pump pulse. Both will cover the same frequency range and so the unwanted 2nd-order SFG field cannot be removed by filtering. In addition, there is the second-order non-resonant field $E_{nonres}^{(2)}(\omega_3,t_1,t_2)$, which in our experiments we use as our local oscillator pulse. On the detector, all three of these fields will interfere, giving the measured signal:

$$\begin{aligned} S(\omega_3,t_1,t_2) &= \left|E_{res}^{(2)} + E_{nonres}^{(2)} + E_{res}^{(4)}\right|^2 \equiv \left|E_{res}^{(2)} + E_{LO}^{(2)} + E_{res}^{(4)}\right|^2 \\ &= \left|E_{res}^{(2)}\right|^2 + \left|E_{LO}^{(2)}\right|^2 + \left|E_{res}^{(4)}\right|^2 + 2E_{res}^{(2)}E_{LO} + 2E_{res}^{(4)}E_{res}^{(2)} + 2E_{res}^{(4)}E_{LO} \end{aligned} \quad (1)$$

The cross terms E_iE_j in Equation (1) depend on the phase of the incident laser pulses, which is:

$$\begin{aligned} E_{res}^{(2)}E_{LO} &\sim \cos[\omega t + (\phi_3 + \phi_{vis} + \Delta\phi_{res,nonres}) - (\phi_3 + \phi_{vis})] \\ &\sim \cos(\omega t + \Delta\phi_{res,nonres}) \\ E_{res}^{(4)}E_{LO} &\sim \cos[\omega t + (\phi_3 + \phi_{vis} \pm \Delta\phi_{1,2} + \Delta\phi_{res,nonres}) - (\phi_3 + \phi_{vis})] \\ &\sim \cos(\omega t \pm \Delta\phi_{1,2} + \Delta\phi_{res,nonres}) \\ E_{res}^{(4)}E_{res}^{(2)} &\sim \cos[\omega t + (\phi_3 + \phi_{vis} \pm \Delta\phi_{1,2}) - (\phi_3 + \phi_{vis})] \\ &\sim \cos(\omega t \pm \Delta\phi_{1,2}) \end{aligned} \quad (2)$$

Of these terms, we only want the cross term $E_{res}^{(4)}E_{LO}$, which most faithfully measures the 4th-order electric field because the nonresonant E_{LO} from gold has a well-defined phase $\Delta\phi_{res,nonres}$ with respect to the resonant contribution to the signal and is temporally short[39]. In previous reports, the term $E_{res}^{(4)}E_{res}^{(2)}$ was used to generate a 2D SFG spectrum[40], but that causes problems in spectral interpretation because the 2nd-order signal is a complicated function of amplitude and phase that is

not necessarily well-understood[41]. To obtain our desired term and eliminate the others, we use phase cycling. The phase of a laser pulse is set by the delay of the carrier wave relative to the envelope (see Fig. 3 inset). The different phase dependence above terms as shown in Equation 2 can be utilized to extract our desired signal from the others (inset). For each t_1 delay, the signal is first measured with E_1 and E_2 having phases $\phi_1 = 0$ and $\phi_2 = 0$, respectively, and then $\phi_1 = \pi$ and $\phi_2 = 0$. The two signals are then subtracted. Mathematically, one substitutes ϕ_1 and ϕ_2 into the equations above, which gives

$$S(\Delta\phi_{1,2} = 0) - S(\Delta\phi_{1,2} = \pi) = 4E_{res}^{(4)}E_{LO} + 4E_{res}^{(2)}E_{res}^{(4)} \qquad (3)$$

and contains the term that we want. The second term cannot be removed, but since $E_{LO} \gg E_{res}^{(2)}$, it is much smaller than $E_{res}^{(4)}E_{LO}$, and so we ignore it. Instead of phase cycling, one could also chop the E_1 and E_2 beams, like often done in transient absorption spectroscopy[42]. Phase cycling is preferable, because signal is collected with every laser shot, and thus data collection is effectively twice the repetition rate as chopping. There are several experimental methods for setting the carrier phase, but pulse shaping makes it very easy because it is done by computer programming.

Phase cycling is also used to shift the apparent frequency of the measured 2D SFG signal[28, 43]. For condensed phase peptides, sufficient resolution is achieved by scanning to maximum delays of 1500 to 2500 fs. The Nyquist theorem says that two points per period must be collected to fully sample a sine wave. The peptide vibrations measured here absorb at about 6 microns, which has a period of about 20fs. Thus, step sizes cannot be larger than 9fs to follow the Nyquist theorem, requiring ~170 measurements to reach a maximum delay of 1500 fs. Instead, we take 50 fs steps, but still sample at the Nyquist frequency by shifting the apparent frequency of the measure field to 50 microns, which has a period of 167fs. This is done by using a different phase for E_1 at each delay (in addition to the phase flips described above) that partially counteracts the phase shift caused by the delay itself. Data collection in the rotating frame is commonly used in NMR spectroscopy. Phase cycling makes its application in optical spectroscopies very straightforward to implement.

Coupled vibrations and simulations of the 2D SFG spectra

To explore possible structures that might explain the experimental 2D SFG spectra presented below, we have simulated the 2D SFG spectra using an excitonic coupling model and the formalism for heterodyne detected 2D SFG spectroscopy. The ester monolayer is built by arranging MMB into a close packed array. Each ester is oriented such that the C3-S13 bond aligns with surface normal and the benzene ring lies on X-Z plane. The structure, transition dipole and Raman tensor are calculated by Gaussian 09. The amyloid fibers are built assuming standard dihedral angles for a β-strand and then arranging them into parallel β-sheets. Transition dipole coupling is used to describe all coupling elements. The nearest-neighbor interactions are

modeled separately by a coupling constant of 0.8 cm^{-1}, since a transitional dipole couplings model is known to overestimate the couplings of nearest neighbors in peptides[44]. For the peptide, each amide bond is assigned a transition dipole that is oriented 20^o from the carbonyl bound[45]. The amide transition dipole is approximated to be equal in magnitude to the ester dipole for simplicity. A similar procedure is used for the polarizability tensors. The fundamental frequency for the amides is set to $1700cm^{-1}$ and for the esters at $1745cm^{-1}$. The anharmonic shift of all stretches is approximated as $20cm^{-1}$. From these parameters, 1-quantum and 2-quantum Hamiltonians are built and diagonalized to obtain the transition dipoles and directions of the excitons. These quantities are then input into the Feynman path formalism form which the 2D SFG spectra are generated[36].

Preparation of the monolayer and peptide samples

Peptide synthesis

The FGAIL pentapeptide was obtained from a 0.1 mmol scale solid-phase synthesis using standard FMOC chemistry[46], with double 2 hr couplings of each amino acid. PAL-PEG-PS resin was employed in order to generate an amidated C-terminus. The resin was cleaved for 4 hrs in 95% (v/v) TFA in H_2O. Crude peptide was then purified by reverse phase HPLC and verified by mass using electrospray ionization mass-spectrometry.

Preparation of MMB monolayers on gold

Methyl 4-mercaptobenzoate (MMB) was obtained from Toronto Research Chemicals Inc. and used without further purification. The MMB monolayers on gold were deposited using established protocols[47, 48]. Fresh gold substrates (Platypus Technologies – 100 nm Au with 5 nm Ti adhesion layer on silicon <1,0,0> wafers, ~1cm X 1cm dimension) were soaked in 1mM MMB solutions in methanol (Sigma Aldrich, HPLC grade, 99.9%) for 24 hours. The substrates were then removed from solution, rinsed thoroughly with pure methanol and dried under nitrogen. The samples were then used for the 2D-SFG measurements. For the deposition of FGAIL, ester coated gold substrates were prepared as described above, following which a 400μM solution of FGAIL was added on the substrate and dried.

Results

Shown in Fig. 4A is the heterodyne detected 2D SFG spectrum of methyl 4-mercaptobenzoate (MMB) on gold for $t_2 = 0$. Three strong peaks are observed, labeled in Fig. 4A as “A”, “B” and “C”. Peaks A and B appear at

$\{\omega_{pump},\omega_{probe}\}=\{1740\ cm^{-1},1742cm^{-1}\}$ and $\{1740\ cm^{-1},1714cm^{-1}\}$. These peaks are caused by transitions to the fundamental and overtone states, as described above, and so their difference in frequency is caused by the anharmonic shift (the actual anharmonic shift is smaller than the peak separation because the picosecond pulse broadens the spectra along the x-axis)[37]. Peak C has not been observed in previous 2D SFG spectra. It may arise from a distribution of eigenstates caused by coupling between esters, as suggested by simulations presented below. The noise level in this spectrum is about one contour level, and so only peaks A, B and C lie appreciably above the noise.

The 2D SFG spectrum of the monolayer soaked in a solution of FGAIL peptide is shown in Fig. 4B. It exhibits peaks A, B and C, as observed in Fig. 4A for the ester stretches of the MMB monolayers. In addition, there are peaks that we label D, E and F, as well as other features above the noise level. The 2D SFG spectrum of the MMB monolayer did not have any features in the region of these three peaks. Thus, we conclude that peaks A, B and C arises from the amide vibrations of adsorbed peptide on MMB. That is an interesting observation because samples made by soaking gold substrates in 400μM aqueous FGAIL solution without the MMB monolayer produced no measureable signal (data not shown) even though the surface was clearly coated with peptide (by visual inspection). Thus, the MMB monolayer is necessary to create ordered protein conformations, which is a point that we come back to in the Discussion.

In addition to peaks D, E and F, we also mark 3 other features that are above the noise, labeled G, H and I. Peak G also lies below the frequency range observed for the MMB esters, and so we assign it to a cross peak associated with FGAIL. Peak H lies above A, B or C. We believe it is diagonal peak of the MMB mode causing peak C. Finally, peak I appears to correlate peak H with peak E, making it a cross peak between the ester stretches and the FGAIL peptide.

Simulations of MMB and MMB-FGAIL 2D SFG spectra

Shown in Fig. 5 are simulated spectra of the MMB monolayer, and the monolayer with a 4-stranded parallel *β*-sheet in two different orientations. The MMB monolayer exhibits features similar to peaks A, B and C. Examination of the eigenvectors that produce the peaks reveals that peak C is caused by coupling between bright and dark eigenstates, although it is much weaker in the simulations than experiment.

The peptide features all appear at lower frequencies than MMB. In the perpendicular orientation (Fig. 5b), the *β*-strands of the amyloid fiber stand up straight from the monolayer so that the fiber axis lies along the surface whereas in the parallel orientation the strands lie on the MMB monolayer so that the fiber axis points away from the surface. The 2D SFG spectra for the peptide are very different in these two orientations. Parallel *β*-sheets have an a^- mode that runs across the *β*-

strands and an a^+ mode that lies (somewhat) along the strands[37, 49]. The a^- mode absorbs 50-60 cm^{-1} lower than the a^+ mode and usually dominates an IR spectrum because its transition dipole is much larger. That is not the case in the perpendicular orientation simulated here. Since the a^- mode lies along the surface, it is only weakly SFG active whereas the a^+ mode lies in an orientation that produces the strongest SFG signal. Thus, both modes have above equal intensity in this orientation and produce strong cross peaks between them. In the parallel orientation (Fig. 5a), it is the a^+ mode that is SFG inactive and the a^- mode pointing perpendicular to the surface, making its intensity dominate.

Both simulated spectra predict cross peaks between the ester stretches and the peptides. Thus, the vibrational coupling is larger enough to become delocalized across the interface. It is also interesting to note that the peptides alter the features of the MMB itself, producing a peak similar to peak C from the experiments.

Discussion

The data presented in this study make it clear that the membranes are playing an active role in fiber orientation, if not their growth. No SFG signal is observed for bare gold surfaces, even though dried peptide deposits are observed. Thus, the gold surface does not orient the molecules and any amyloid fibers formed in solution deposit onto the surface randomly. With MMB present, very strong SFG signals are observed, indicating ordering. Control experiments will have to be performed to determine if the peptides are aggregating in solution and then ordering upon binding to MMB or if the MMB causes amyloid fibers to growing on the surface. Based on literature reports, we believe the latter. Many interfaces cause amyloid fiber aggregation. Lipid interfaces typically cause amyloid aggregation many times faster than observed in solution, making surface aggregation the dominant process[10, 50]. Thus, we believe that the MMB surface either binds the FGAIL monomers, thereby increasing their concentration and accelerating aggregation, or serving to nucleate a particular structure that can seed fiber formation. Either way, the mechanism must be uniform, since the process results in well-ordered β-sheets.

Neither of the simulations presented here match the experimental spectrum well-enough to be representative of the true molecular structure, but the simulations do help their interpretation. First, the simulations show that the ratio of the a^- and a^+ modes will depend on the β-sheet orientation. The experiments have a stronger a^- mode (peak D) and the phase of the a^- mode and the ester stretch (B) are both positive, suggesting that the β-strands are largely parallel to the surface so that the amyloid β-sheets grow away from the surface. With that interpretation, peak G would be a cross peak between the a^- and a^+ modes, albeit more intense than predicted in the simulations. Qualitatively, it appears that the FGAIL peptides bind in a linear conformation to the surface, like shown in Fig. 5b.

The simulations also seem to support the assignment of peak I to a cross peak

between the ester and the peptide. In the simulations the coupling is large enough to create cross peaks between the two. However, cross peaks appear in both FGAIL orientations, and so it is not clear how to interpret the magnitude of the peak I. The fact that peak I is correlating the a^- mode of the β-sheet to an MMB mode that is normally forbidden, may be a consequence of the peptide disordering the MMB monolayer. Disorder will break the 2D symmetry and redistribute oscillator strength, thereby making forbidden MMB modes more intense. Amyloid fiber formation is known to disrupt lipid monolayers[51, 52]. The cross peaks certainly indicate hydrogen bonding between the esters of MMB and the peptide backbone.

Many other factors needs to be taken into account for more reliable simulations. For example, the coupling model used to calculate these numbers has not been calibrated for ester stretches, and so the magnitude of these couplings may be wrong. The monolayer structure is assumed to be well-ordered, whereas structural disorder is probably present. Presumably, the ester stretches will not all point in the same direction like they do in our simulations. Moreover, the relative surface coverages of MMB and FGAIL also need to be evaluated, as the surface density dictates into the SFG signal intensity. Nevertheless, simulations like these are able to reproduce experimental 2D IR and 2D SFG spectra reasonably well and to discriminate between possible structures. We expect the same to be ultimately true here as well.

Conclusions

Surfaces play an important role in catalyzing amyloid fiber formation, yet the mechanism and resulting structures are largely unknown. In this paper, we show that we can collect 2D SFG spectra of amyloid peptides formed by an ester monolayer. The spectra clearly resolve β-sheets that are consistent with amyloid fiber formation and a comparison with simulations suggests that the fiber axis is perpendicular to the surface. Although these results are still preliminary, if this conclusions holds, then it may indicate that the surface promotes seed formation by aligning the FGAIL peptides into strands parallel to the surface that then nucleate fiber growth. Further experiments are needed to test this hypothesis. 2D IR spectroscopy has become an important tool for studying peptide and amyloid structures. Extension of these techniques to surface monolayers opens up a new realm of experiments.

Acknowledgements

The authors thank the National Science Foundation (NSF) for funding through Grant CHE-1266422. Funding for A.L.S. was provided by a Diversity Supplement to NIH DK079895. D.R.S. was supported by the University of Wisconsin Materials Research Science and Engineering Center (UW-MRSEC, DMR-1121288).

Figures:

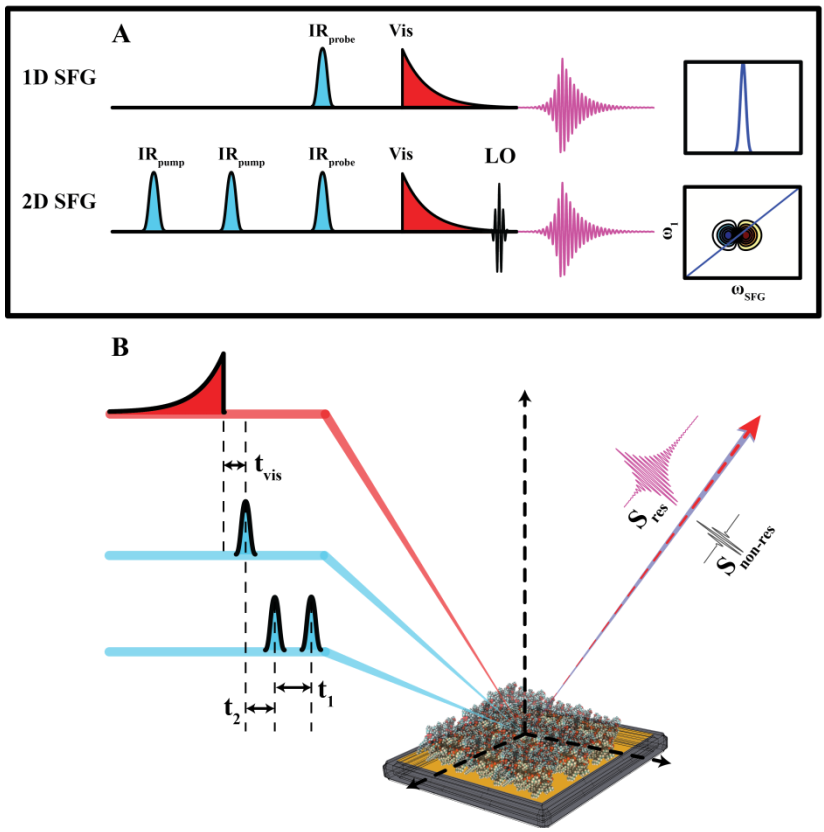

Figure 1:

A. Outline of the pulse sequence used in the 1D and 2D SFG experiments.

B. Schematic of the beam geometry in 2D SFG experiments. All pulses are p-polarized. t_1, t_2 and t_{vis} denote the delays between the two mid-IR pump pulses, between the pump and probe mid-IR pulses and the probe and visible pulses respectively.

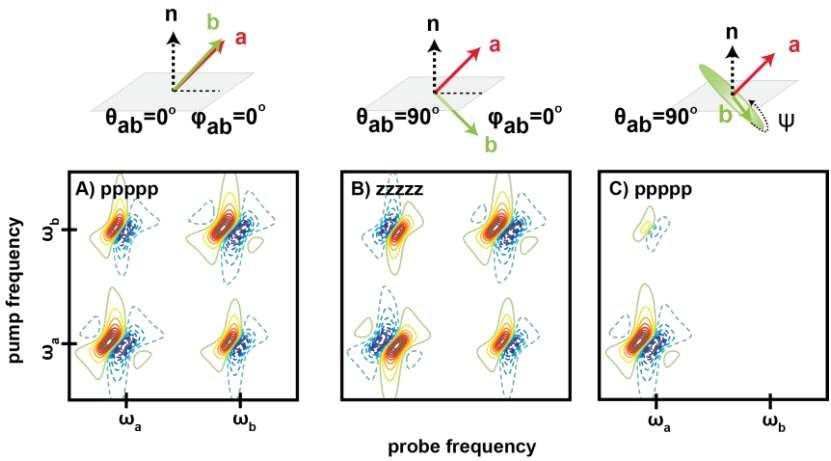

Figure 2:

Simulated 2D SFG spectra for a model system of two coupled oscillators for different orientations and polarization conditions. (A.) The relative angle between the modes is set to zero. Spectra are calculated for the ppppp polarization condition. (B.) The relative angle between the modes is zero, but they have different tilt angles (θ_{ab} = 90°) with respect to the surface normal. Spectra are calculated for zzzzz polarization. (C.) 2D SFG spectra for a ϕ- and ψ-averaged system. The mode a is assumed to lie along the rotation axis. Spectra are calculated using all p-polarized pulses. (Adapted from ref. 36)

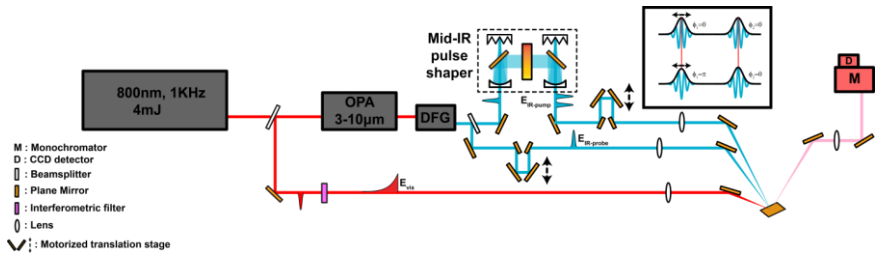

Figure 3:

Schematic layout of the 2D SFG experimental setup. The phase cycling procedure adopted in the experiments is illustrated in the inset.

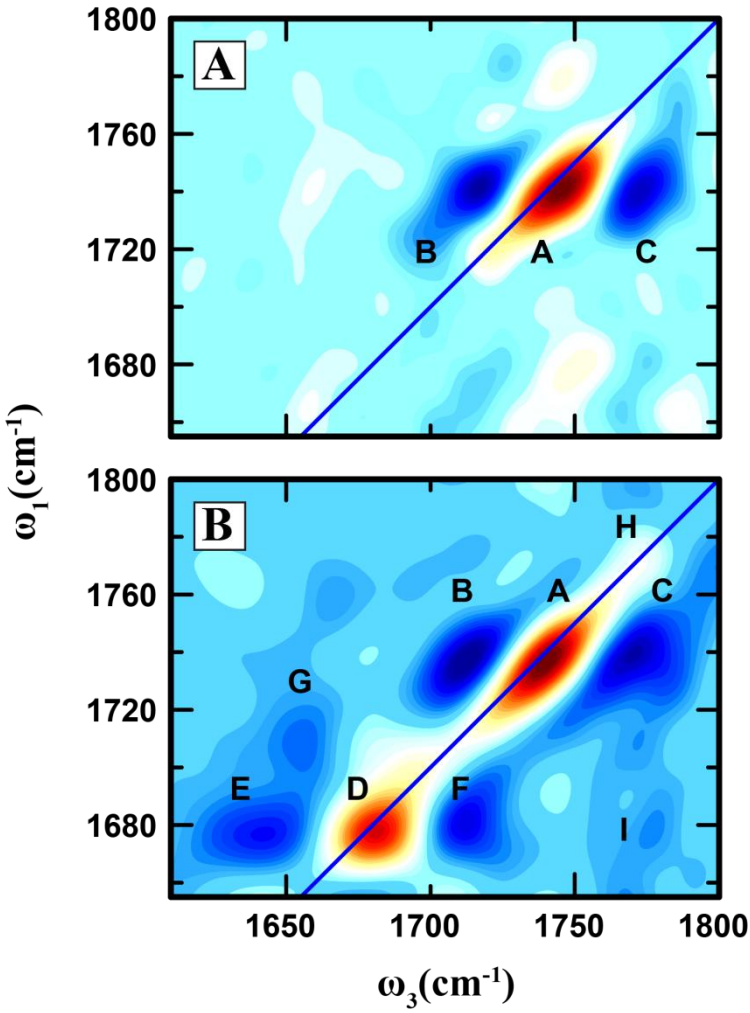

Figure 4:

Experimental 2D SFG spectra at $t_2 = 0$ of (A) MMB monolayers on gold substrates and (B) FGAIL on MMB coated gold substrates.

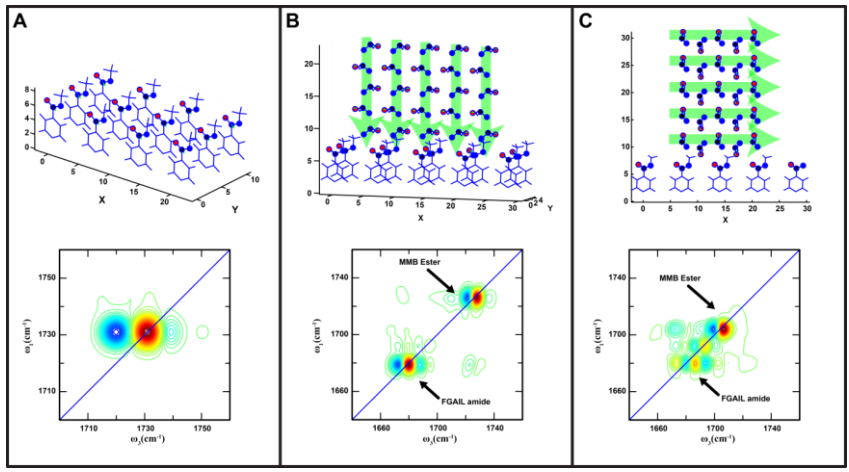

Figure 5:

Simulated 2D SFG spectra for MMB monolayers with and without adsorbed FGAIL.

(A) MMB monolayer. (B) FGIAL-MMB, with the fibril axis parallel to the monolayer. (C) FGAIL-MMB, with the fibril axis perpendicular to the monolayer

References

1. D. Eisenberg and M. Jucker, *Cell*, 2012, **148**, 1188-1203.
2. P. Westermark, U. Engström, K. H. Johnson, G. T. Westermark and C. Betsholtz, *Proceedings of the National Academy of Sciences*, 1990, **87**, 5036-5040.
3. C. Betsholtz, L. Christmansson, U. Engström, F. Rorsman, V. Svensson, K. H. Johnson and P. Westermark, *FEBS Lett.*, 1989, **251**, 261-264.
4. K. Tenidis, M. Waldner and J. Bernhagen, *J. Mol. Biol*, 2000, **295**, 1055-1071.
5. T. T. Ashburn, M. Auger and P. T. Lansbury, *J. Am. Chem. Soc.*, 1992, **114**, 790-791.
6. G. G. Glenner, E. David Eanes and C. A. Wiley, *Biochem. Biophys. Res. Commun.*, 1988, **155**, 608-614.
7. Y. Porat, Y. Mazor, S. Efrat and E. Gazit, *Biochemistry*, 2004, **43**, 14454-14462.
8. S. Luca, W.-M. Yau, R. Leapman and R. Tycko, *Biochemistry*, 2007, **46**, 13505-13522.
9. L. E. Buchanan, E. B. Dunkelberger, H. Q. Tran, P.-N. Cheng, C.-C. Chiu, P. Cao, D. P. Raleigh, J. J. de Pablo, J. S. Nowick and M. T. Zanni, *Proceedings of the National Academy of Sciences*, 2013, **110**, 19285-19290.
10. J. D. Knight and A. D. Miranker, *J. Mol. Biol.*, 2004, **341**, 1175-1187.
11. S. A. Jayasinghe and R. Langen, *Biochemistry*, 2005, **44**, 12113-12119.
12. J. D. Knight, J. A. Hebda and A. D. Miranker, *Biochemistry*, 2006, **45**, 9496-9508.
13. J. Adamcik, J.-M. Jung, J. Flakowski, P. De Los Rios, G. Dietler and R. Mezzenga, *Nat Nano*, 2010, **5**, 423-428.
14. T. Kowalewski and D. M. Holtzman, *Proceedings of the National Academy of Sciences*, 1999, **96**, 3688-3693.
15. W. Qiang, K. Kelley and R. Tycko, *J. Am. Chem. Soc.*, 2013, **135**, 6860-6871.
16. C. Wu, H. Lei and Y. Duan, *J. Am. Chem. Soc.*, 2005, **127**, 13530-13537.
17. A. Melquiond, J.-C. Gelly, N. Mousseau and P. Derreumaux, *The Journal of Chemical Physics*, 2007, **126**, -.
18. D. Zanuy, Y. Porat, E. Gazit and R. Nussinov, *Structure*, 2004, **12**, 439-455.
19. A. Kapurniotu, A. Schmauder and K. Tenidis, *J. Mol. Biol.*, 2002, **315**, 339-350.
20. M. Tatarek-Nossol, L.-M. Yan, A. Schmauder, K. Tenidis, G. Westermark and A. Kapurniotu, *Chem. Biol.*, 2005, **12**, 797-809.
21. J. J. W. Wiltzius, S. A. Sievers, M. R. Sawaya, D. Cascio, D. Popov, C. Riekel and D. Eisenberg, *Protein Sci.*, 2008, **17**, 1467-1474.
22. C. P. Shaw, D. A. Middleton, M. Volk and R. Lévy, *ACS Nano*, 2012, **6**, 1416-1426.
23. D. Zanuy, B. Ma and R. Nussinov, *Biophys. J.*, 2003, **84**, 1884-1894.
24. Y. R. Shen, *J. Phys. Chem. C*, 2013, **117**, 11884-11884.
25. Y. R. Shen, *The principles of nonlinear optics*, Wiley classics library edn., Wiley-Interscience, Hoboken, N.J., 2003.
26. Y. R. Shen and V. Ostroverkhov, *Chem. Rev. (Washington, DC, U. S.)*, 2006, **106**, 1140-1154.
27. A. G. Lambert, P. B. Davies and D. J. Neivandt, *Appl. Spectrosc. Rev.*, 2005, **40**, 103-145.
28. W. Xiong, J. E. Laaser, R. D. Mehlenbacher and M. T. Zanni, *Proc. Natl. Acad. Sci. U. S. A.*, 2011, **108**, 20902-20907.
29. A. M. Jubb, W. Hua and H. C. Allen, *Acc. Chem. Res.*, 2012, **45**, 110-119.
30. L. Fu, G. Ma and E. C. Y. Yan, *J. Am. Chem. Soc.*, 2010, **132**, 5405-5412.
31. I. V. Stiopkin, H. D. Jayathilake, A. N. Bordenyuk and A. V. Benderskii, *J. Am. Chem. Soc.*, 2008, **130**, 2271-2275.
32. S. H. Shim, D. B. Strasfeld, Y. L. Ling and M. T. Zanni, *Proc. Natl. Acad. Sci. U. S. A.*, 2007, **104**, 14197-14202.
33. P. Hamm, M. H. Lim and R. M. Hochstrasser, *J. Phys. Chem. B*, 1998, **102**, 6123-6138.
34. M. T. Zanni, N. H. Ge, Y. S. Kim and R. M. Hochstrasser, *Proc. Natl. Acad. Sci. U. S. A.*, 2001, **98**, 11265-11270.
35. M. Khalil, N. Demirdoven and A. Tokmakoff, *Phys. Rev. Lett.*, 2003, **90**.
36. J. E. Laaser and M. T. Zanni, *J. Phys. Chem. A*, 2013, **117**, 5875-5890.
37. J. E. Laaser, D. R. Skoff, J. J. Ho, Y. Joo, A. L. Serrano, J. D. Steinkruger, P. Gopalan, S. H. Gellman and M. T. Zanni, *J. Am. Chem. Soc.*, 2014, **136**, 956-962.
38. D. R. Skoff, Ho Jia-Jung, Ghosh Ayanjeet, Zanni Martin T., *In preparation*.
39. A. Lagutchev, S. A. Hambir and D. D. Dlott, *The Journal of Physical Chemistry C*, 2007, **111**, 13645-13647.

40. S. Nihonyanagi, J. A. Mondal, S. Yamaguchi and T. Tahara, *Annu. Rev. Phys. Chem.*, 2013, **64**, 579-603.
41. M. Cho, *Two-dimensional optical spectroscopy*, CRC Press, Boca Raton, 2009.
42. P. Hamm and M. T. Zanni, *Concepts and methods of 2d infrared spectroscopy*, Cambridge University Pres, Cambridge ; New York, 2011.
43. S.-H. Shim and M. T. Zanni, *Phys. Chem. Chem. Phys.*, 2009, **11**, 748-761.
44. C. Lee and M. H. Cho, *J. Phys. Chem. B*, 2004, **108**, 20397-20407.
45. W. H. Moore and S. Krimm, *Biopolymers*, 1976, **15**, 2439-2464.
46. P. Marek, A. M. Woys, K. Sutton, M. T. Zanni and D. P. Raleigh, *Org. Lett.*, 2010, **12**, 4848-4851.
47. A. Michota and J. Bukowska, *J. Raman Spectrosc.*, 2003, **34**, 21-25.
48. J. C. Love, L. A. Estroff, J. K. Kriebel, R. G. Nuzzo and G. M. Whitesides, *Chem. Rev. (Washington, DC, U. S.)*, 2005, **105**, 1103-1170.
49. C. M. Cheatum, A. Tokmakoff and J. Knoester, *The Journal of Chemical Physics*, 2004, **120**, 8201-8215.
50. Y. L. Ling, D. B. Strasfeld, S. H. Shim, D. P. Raleigh and M. T. Zanni, *J. Phys. Chem. B*, 2009, **113**, 2498-2505.
51. E. Sparr, M. F. M. Engel, D. V. Sakharov, M. Sprong, J. Jacobs, B. de Kruijff, J. W. M. Höppener and J. Antoinette Killian, *FEBS Lett.*, 2004, **577**, 117-120.
52. M. Anguiano, R. J. Nowak and P. T. Lansbury, *Biochemistry*, 2002, **41**, 11338-11343.